

# Unified equations of state for cold nonaccreting neutron stars with Brussels-Montreal functionals.

## II. Pasta phases in semiclassical approximation

J. M. Pearson,<sup>1</sup> N. Chamel,<sup>2</sup> and A. Y. Potekhin<sup>3</sup>

<sup>1</sup>*Département de Physique, Université de Montréal, Montréal, Québec, Canada H3C 3J7*

<sup>2</sup>*Institut d'Astronomie et d'Astrophysique, CP-226, Université Libre de Bruxelles, 1050 Brussels, Belgium*

<sup>3</sup>*Ioffe Institute, Politekhnikeskaya 26, 194021 Saint Petersburg, Russia*



(Received 9 September 2019; published 15 January 2020)

We generalize our earlier work on neutron stars, which assumed spherical Wigner-Seitz cells in the inner crust, to admit the possibility of pasta phases, i.e., nonspherical cell shapes. Full fourth-order extended Thomas-Fermi (ETF) calculations using the density functional BSk24 are performed for cylindrical and platelike cells. Unlike in our spherical-cell calculations we do not include shell and pairing corrections, but there are grounds for expecting these corrections for pasta to be significantly smaller. It is therefore meaningful to compare the ETF pasta results with the full spherical-cell results, i.e., with shell and pairing corrections included. However, in view of the many previous studies in which shell and pairing corrections were omitted entirely, it is of interest to compare our pasta results with the ETF part of the corresponding spherical calculations. Making this latter comparison, we find that as the density increases the cell shapes pass through the usual sequence sphere  $\rightarrow$  cylinder  $\rightarrow$  plate before the transition to the homogeneous core. The filling fractions found at the phase transitions are in close agreement with expectations based on the liquid-drop model. On the other hand, when we compare with the full spherical-cell results, we find the sequence to be sphere  $\rightarrow$  cylinder  $\rightarrow$  sphere  $\rightarrow$  cylinder  $\rightarrow$  plate. In neither case do any “inverted,” i.e., bubblelike, configurations appear. The analytic fitting formulas for the equation of state and composition that we derived in our earlier work, with the assumption of spherical cell shapes for the entire density range from the outer crust to the core of a neutron star, are found to remain essentially unchanged for pasta shapes. Here, however, we provide more accurate fitting formulas to all our essential numerical results for each of the three phases, designed especially for the density range where the nonspherical shapes are expected, which enable one to capture not only the general behavior of the fitted functions but also the differences between them in different phases.

DOI: [10.1103/PhysRevC.101.015802](https://doi.org/10.1103/PhysRevC.101.015802)

### I. INTRODUCTION

Working within the framework of the theory of nuclear energy-density functionals, we recently published calculations of the equation of state (EoS) and the composition of the ground state of neutron-star matter that are unified in the sense that all three major regions of these stars are treated using the same functional [1] (paper I of this series). The importance of such a unified treatment has been discussed, e.g., in Refs. [2–7].

The outermost of the three regions, the “outer crust,” consists of an assembly of bound nuclei and electrons that globally is electrically neutral. The nuclei in this region become more and more neutron rich with increasing depth, until at a mean baryon number density  $\bar{n}$  of around  $2.6 \times 10^{-4} \text{ fm}^{-3}$  unbound neutrons appear. This so-called “neutron drip” marks the transition to the “inner crust,” an inhomogeneous assembly of neutron-proton clusters and unbound neutrons, neutralized by electrons. As shown in Ref. [1], at much higher densities a substantial amount of free protons may appear, which is called “proton drip” because of the analogy (albeit incomplete) with the neutron drip. By the point where  $\bar{n}$  has risen to about

$0.08 \text{ fm}^{-3}$  the inhomogeneities have been smoothed out: this is the “core” of the star.

The calculations of Ref. [1] were actually performed with four different functionals, each functional being used in all three regions of the neutron star. These functionals, labeled BSk22, BSk24, BSk25, and BSk26, belong to a family of functionals that have been developed not only for the study of neutron-star structure but also for the general purpose of providing a unified treatment of a wide variety of phenomena associated with the birth and death of neutron stars, such as supernova-core collapse and neutron-star mergers, along with the  $r$  process of nucleosynthesis (Ref. [8] and references therein). They are based on generalized Skyrme-type forces and density-dependent contact pairing forces, the formalism for which is presented in Refs. [9,10]. The parameters of the functionals were determined primarily by fitting to essentially all the nuclear-mass data of the 2012 Atomic Mass Evaluation [11]; we calculated nuclear masses using the Hartree-Fock-Bogoliubov (HFB) method, with axial deformation taken into account. In making these fits we imposed certain constraints, the most significant of which is to require consistency, up to the densities prevailing in neutron-star cores, with the EoS

of homogeneous pure neutron matter, as calculated by many-body theory from realistic two- and three-nucleon forces.

For the nuclear masses required for the treatment of the outer crust in Ref. [1] we took experimental values, where available, and otherwise used the values determined by HFB calculations with the appropriate functional. In the interest of consistency it might appear desirable to apply this same method to the inner crust, but this would require unacceptably long computer times; see, e.g., Ref. [12] for a recent summary of the situation. Instead, we adopted the ETFSI (fourth-order extended Thomas-Fermi plus Strutinsky integral) method [13–16]. It consists of a full ETF treatment of the kinetic-energy and spin-current densities, with shell corrections added perturbatively and pairing handled in the Bardeen-Cooper-Schrieffer (BCS) approximation. It is to be noted that the errors incurred by the latter approximation lie within the errors of the ETFSI approach [17]. The ETFSI+BCS method was originally developed for the treatment of bound nuclei [18], and we discuss in Ref. [1] the high degree of accuracy with which it approximates the HF+BCS method in that context. When applied to the calculation of the EoS of the inner crust we take only the proton shell corrections into account. The neutron shell corrections have been shown to be much smaller than the proton shell corrections [19], as might be expected, given that the spectrum of unbound neutron single-particle (s.p.) states is continuous [20,21]. We thus simply neglect the neutron shell corrections, an option that is not available in the HFB method but is possible in the ETFSI method because of its perturbative treatment of these corrections. We likewise include proton pairing [16] but not neutron pairing.

Our ETFSI calculations of the inner crust have in all our previous work assumed spherically symmetric Wigner-Seitz (WS) cells as an approximate description. Usually, our solutions are droplike, i.e., the density is higher in the center of the cell than at the surface, but in Ref. [1] “inverted” solutions were found at some points close to the interface with the core. In the literature, such “bubblelike” solutions are often accompanied by nonspherical solutions at neighboring densities (see, for example, Ref. [22]). In the present paper we therefore go beyond the assumption of spherical WS cells.

Investigation of nonspherical configurations goes back to the work of Ravenhall *et al.* [23] and Hashimoto *et al.* [24], who considered, as an alternative to spherical shapes, infinitely long cylinders and plates of infinite extent. These are referred to as “spaghetti” and “lasagna” respectively, and thus collectively as “pasta.” Other early papers to be noted are those of Williams and Koonin [25] and Lorenz *et al.* [26]; see also Refs. [12,22] for reviews. The part of the inner crust in which pasta shapes prevail is referred to as the “mantle.” It has been shown to behave like liquid crystals [27], in contrast to the rest of the inner crust, which can be regarded as a solid. Early studies of the pasta phases were formulated in terms of the liquid-drop model, but even within the framework of energy-density functional theory the question as to whether or not nonspherical shapes can ever be energetically favored is still a matter of some controversy. For example, the second-order ETF calculations of Ref. [28] with parametrized nucleon distributions show a transition to nonspherical shapes at a density  $\bar{n}$  close to  $0.06 \text{ fm}^{-3}$  in the inner crust for the

functional SLy4, while the zeroth-order TF calculations of Ref. [29] with the same functional yield no deviation from a spherical shape.

We present in this paper what we believe to be the first full fourth-order ETF calculations of pasta within the WS approach. However, of the four functionals considered in Ref. [1] we limit ourselves here to the phenomenologically superior BSk24 (see Ref. [8]). In Sec. II we describe our method of calculating cylindrical and platelike WS cells, while our results are summarized in Sec. III. The conclusions will be found in Sec. IV. In the Appendix we provide proofs of some equations used in the main text. Extended numerical results are presented as Supplemental Material [30] in electronic form.

## II. CALCULATION OF PASTA PHASES

We draw here heavily on our earlier work on spherical WS cells [1,14,15,31], emphasizing mainly the ways in which it has to be modified for pasta calculations. For both the infinitely long cylindrically symmetric WS cells of the “spaghetti” phase and the platelike WS cells of infinite extent representing the “lasagna” phase we still write for the total energy per nucleon

$$e = e_{\text{Sky}} + e_{\text{C}} + e_e - Y_p Q_{n,\beta}. \quad (1)$$

Here the first term denotes the total nuclear energy per nucleon corresponding to our chosen Skyrme functional, the second and third terms the Coulomb and electronic kinetic energy per nucleon, respectively, while the last term takes account of the neutron-proton mass difference,  $Q_{n,\beta}$  ( $=0.782 \text{ MeV}$ ) being the beta-decay energy of the neutron. In this last term  $Y_p$  is the proton fraction  $Z/A$ ,  $Z$  and  $A$  being respectively the number of protons and nucleons in the WS cell for the spherical case, the number per unit length of cylindrical cells, or the number per unit area of platelike cells. (We have dropped for convenience the constant neutron mass term  $M_n c^2$ .) The electronic term  $e_e$  is the same for all geometries, and therefore is as in Ref. [1]. We now examine in detail the first two terms.

### A. Skyrme energy

The first term of Eq. (1) can be written as an integral over the cell of an energy density  $\mathcal{E}_{\text{Sky}}(\mathbf{r})$ , thus

$$e_{\text{Sky}} = \frac{1}{A} \int_{\text{cell}} \mathcal{E}_{\text{Sky}}(\mathbf{r}) d^3\mathbf{r}; \quad (2)$$

in the case of cylindrical shapes the integration is taken over unit length, and in the case of plates over unit area. For our generalized Skyrme functionals the energy density  $\mathcal{E}_{\text{Sky}}(\mathbf{r})$  is given by Eq. (A3) of Ref. [9] in terms of the number densities  $n_q(\mathbf{r})$ , the kinetic-energy densities  $\tau_q(\mathbf{r})$ , and the spin-current densities  $\mathbf{J}_q(\mathbf{r})$ , where  $q = p$  or  $q = n$  denotes protons or neutrons, respectively. Note that all the functionals used in Ref. [1] drop the quadratic terms in the spin current (thus removing spurious instabilities [32]), along with the Coulomb exchange term for protons [8]; dropping this latter term leads to a significant improvement in the mass fits, especially mirror-nucleus differences, and can be interpreted

as simulating neglected effects such as Coulomb correlations, charge-symmetry breaking of the nuclear forces, and vacuum polarization [33]. The ETF method then approximates  $\tau_q(\mathbf{r})$  and  $\mathbf{J}_q(\mathbf{r})$  as functions of the number densities  $n_q(\mathbf{r})$  and their derivatives; for a convenient summary of the relevant ETF expressions of Refs. [34,35] see the Appendix of Ref. [31]. However, when  $\mathcal{E}_{\text{Sky}}$  is replaced by its ETF approximation  $\mathcal{E}_{\text{Sky}}^{\text{ETF}}$  all shell effects are lost; the ETFSI method restores them perturbatively, as well as adding a pairing correction. We then have

$$e_{\text{Sky}}^{\text{ETFSI}} = \frac{1}{A} \left\{ \int_{\text{cell}} \mathcal{E}_{\text{Sky}}^{\text{ETF}}(\mathbf{r}) d^3\mathbf{r} + E_p^{\text{sc,pair}} + E_{\text{pair}} \right\}, \quad (3)$$

in which  $E_p^{\text{sc,pair}}$  is the Strutinsky-integral shell correction, as modified by pairing, and  $E_{\text{pair}}$  is the BCS energy [16].

To further speed up the computations, we avoid solving the Euler-Lagrange equations by parametrizing the neutron and proton density distributions  $n_q(\mathbf{r})$ . We adopt a simple generalization of the form taken in the spherical calculations [14], with a sum of a constant ‘‘background’’ term and a ‘‘cluster’’ term according to

$$n_q(\xi) = n_{Bq} + n_{\Lambda q} f_q(\xi), \quad (4)$$

in which

$$f_q(\xi) = \frac{1}{1 + \exp\left[\left(\frac{C_q - R}{\xi - R}\right)^2 - 1\right] \exp\left(\frac{\xi - C_q}{a_q}\right)} \quad (5)$$

and  $\xi$  denotes the radial coordinate  $r$  in the case of spherical cells, the radial coordinate  $\eta$  in the case of cylindrical cells, and  $z$ , the Cartesian coordinate for plates, assumed to lie in the  $x$ - $y$  plane. The parameter  $R$  likewise represents the radius of the spherical cell, the radius of the cylindrical cell, or the semithickness of the platelike cell. At  $\xi = C_q$ ,  $f_q = 1/2$ , whence the parameter  $C_q$  has the meaning of a characteristic size of a nuclear cluster or ‘‘bubble,’’ the latter being a local depletion of the nucleon density below the background level  $n_{Bq}$ , which occurs if  $n_{\Lambda q} < 0$ .

Evaluation of the integral appearing in Eq. (3) then proceeds in exactly the same way for the pasta phases as for the spherical case, except that the expressions for the volume element in the integral, the gradient, and the Laplacian that occur in the ETF expansion have to be chosen appropriately.

The parametrization (5) suffers from the formal defect of a kink at the origin  $\xi = 0$ . The actual density distributions, of course, show no such discontinuity in their derivatives, but no problem will arise with our numerical integrations (performed with the Gauss-Legendre method), provided the mesh size is not too small. We find, in fact, that the computed values of the integrals remain stable against a reduction of the mesh size down to 0.01 fm, one hundredth of the nucleon radius; our final computations were made with a mesh size of 0.1 fm. The integrals thus calculated correspond to the kink in the parametrization (5) having been smoothed out locally, over the region  $0 < \xi \lesssim 0.01$  fm.

The argument for neglecting neutron shell corrections in the spherical-cell calculations [1] is equally valid here. However, while in the spherical-cell calculations of Ref. [1] we did calculate the proton shell corrections, we are not yet able to calculate them for nonspherical cell geometries. Actually, we

argued in Ref. [1] that once proton drip sets in the unbound proton s.p. states will form a quasicontinuum, and proton shell effects should largely vanish, exactly as do neutron shell effects at all densities in the inner crust, i.e., beyond the neutron drip point. We therefore adopted in Ref. [1] the prescription of dropping the proton shell corrections above the proton drip point, and the pairing corrections along with them.

Now even for nonspherical cells the density  $\bar{n}$  at the proton drip point is easily determined. Classically (neglecting quantum tunneling), for protons to be able to escape, their chemical potential  $\mu_p$  must be greater or equal to the proton s.p. field at the cell surface:

$$\mu_p \geq U_p(\xi = R) + M_p c^2. \quad (6)$$

The former quantity is easily calculated by Eqs. (7) and (8) of Ref. [1], since the necessary condition of beta equilibrium is satisfied, while the latter is given by Eq. (A11) of Ref. [9]. (This characterization of the proton drip point is equivalent to the one that we adopted in Ref. [1], but easier to implement.) However, we will see (next section) that once nonspherical shapes are admitted the condition (6) is not satisfied anywhere in the inner crust except perhaps in a narrow region close to the interface with the homogeneous core, at least for the functional BSk24 considered here.

However, there are grounds for expecting proton shell effects to be small for pasta phases, even though the protons may be bound within the WS cell. The point is that in the case of spaghetti the motion along the symmetry axis is unbound, while for lasagna it is the motion in the  $x$ - $y$  plane that is unbound. In both cases the result is that the s.p. proton spectrum is continuous, thus satisfying the criterion we have already been following for neglecting both shell and pairing corrections in the case of neutrons and dripped protons. Some support for this conclusion is found in the recent self-consistent band calculations on lasagna [36]; presumably the shell effects would be somewhat stronger for spaghetti, where the unbounded motion is only one-dimensional. Moreover, these calculations do not include pairing, the effect of which is to dampen the contribution of shell effects on the total binding energy [16]. Thus to the extent that this argument is correct it becomes meaningful to compare the pasta results with the full ETFSI+BCS version of our spherical results.

Another reason to anticipate smallness of the shell corrections in the pasta phases is that there are unbound protons even though Eq. (6) is not satisfied. Note that Eq. (6) assumes classical particle motion, but the proton wave functions at high densities, corresponding to the mantle layers, can substantially penetrate into the neighboring WS cells because of quantum tunneling. In our calculations this effect is mimicked by the background term  $n_{Bp}$  in Eq. (4). While  $n_{Bp}$  is negligibly small at low densities close to the neutron drip, this background term becomes appreciable as  $\bar{n}$  approaches  $n_{cc}$ , where  $n_{cc} \approx 0.08 \text{ fm}^{-3}$  is the number density at the crust-core transition. This leads to increasing number of ‘‘free protons’’  $Z_{\text{free}} \equiv Z - Z_{\text{cl}}$ , where  $Z$  is the total number of protons in the WS cell and  $Z_{\text{cl}}$  is the number of protons clustered near the center.

Nevertheless, the analogy between pasta protons on the one hand and neutrons and dripped protons on the other is

not exact. Because the protons are still bound in their cells their motion in the  $x$ - $y$  plane in the case of spaghetti or along the  $z$  axis in the case of lasagna is still discretized. Thus the continuous s.p. spectrum actually consist of a superposition of continuous s.p. spectra, each one based on a different discrete state. As a result, even though the s.p. spectrum is still continuous, the degeneracy changes discontinuously, and weak shell-model fluctuations can be expected.

To summarize the situation, while it is likely that shell and pairing corrections are smaller for pasta protons than for protons in the spherical configuration, it is far from clear that they will be negligible. Thus in addition to comparing the pasta results with the full ETFSI+BCS version of our spherical results we shall also make the traditional comparison with the ETF version. This is the way in which most previous studies of pasta have been performed (the exceptions include Refs. [19,37,38]). In this way we will acquire some idea of the possible impact of shell and pairing effects in pasta, although no definite conclusion will be possible before they are actually calculated.

### B. Coulomb energy

For the second term in Eq. (1) we denote by  $n_{\text{ch}}(\mathbf{r}) = n_p(\mathbf{r}) - n_e$  the globally neutral charge distribution of protons and electrons in units of the elementary charge  $e$ . Then, as shown in the Appendix, we have the following expressions for the three different geometries.

Spheres:

$$e_C = \frac{8\pi^2 e^2}{A} \int_0^R \left( \frac{u(r)}{r} \right)^2 dr, \quad (7)$$

where

$$u(r) = \int_0^r n_{\text{ch}}(r') r'^2 dr'. \quad (8)$$

Cylinders:

$$e_C = \frac{4\pi^2 e^2}{A} \int_0^R \frac{u(\eta)^2}{\eta} d\eta, \quad (9)$$

where

$$u(\eta) = \int_0^\eta n_{\text{ch}}(\eta') \eta' d\eta'. \quad (10)$$

Plates:

$$e_C = \frac{4\pi e^2}{A} \int_0^R u(z)^2 dz, \quad (11)$$

where

$$u(z) = \int_0^z n_{\text{ch}}(z') dz'. \quad (12)$$

As in all our EoS calculations, a correction for the finite size of the proton is made, as described in Ref. [39].

### III. RESULTS

With the parametrization defined by Eqs. (4) and (5) there are eight independent geometric parameters for given density  $\bar{n}$ , or six if  $Z$  and  $A$  are specified as well. Our computational

TABLE I. Energy per nucleon (in MeV) for different cell shapes; sphere(1) denotes ETF value for spherical shape, sphere(2) denotes same with shell and pairing corrections added. A corresponding optimal shape is denoted by s (spherical), c (cylindrical), and p (platelike).

$\bar{n}$	Cylinder	Plate	Sphere(1)	Sphere(2)
0.0490000	7.00597		7.00575 s	7.00571 s
0.0500000	7.05963		7.05964 c	7.05952 s
0.0510000	7.11249		7.11273 c	7.11254 c
0.0520000	7.16462		7.16506 c	7.16479 c
0.0540000	7.26677		7.26760 c	7.26715 c
0.0560000	7.36638		7.36756 c	7.36692 c
0.0580000	7.46373		7.46521 c	7.46436 c
0.0600000	7.55907		7.56081 c	7.55973 c
0.0610000	7.60605		7.60791 c	7.60670 c
0.0620000	7.65262		7.65458 c	7.65323 c
0.0630000	7.69880		7.70084 c	7.69936 c
0.0640000	7.74460		7.74676 c	7.74509 c
0.0650000	7.79007		7.79226 c	7.79044 c
0.0660000	7.83521		7.83745 c	7.83545 c
0.0670000	7.88005		7.88232 c	7.88011 c
0.0680624	7.92737		7.92967 c	7.92720 s
0.0691445	7.97527		7.97756 c	7.97480 s
0.0692552	7.98016		7.98244 c	7.97965 s
0.0698092	8.00455		8.00682 c	8.00385 s
0.0703677	8.02907		8.03131 c	8.02815 s
0.0709307	8.05371	8.05474	8.05592 c	8.05255 s
0.0714981	8.07847	8.07919	8.08065 c	8.07703 s
0.0720701	8.10336	8.10379	8.10549 c	8.10237 s
0.0726466	8.12836	8.12853	8.13044 c	8.12945 c
0.0732278	8.15350	8.15342	8.15551 p	8.15551 p
0.0738136	8.17877	8.17846	8.18069 p	8.18069 p
0.0744042	8.20416	8.20367	8.20599 p	8.20598 p
0.0749994	8.22968	8.22902	8.23139 p	8.23139 p
0.0755994	8.25531	8.25454	p	p
0.0762042	8.28107	8.28022	p	p
0.0768139	8.30693	8.30603	p	p
0.0774283	8.33289	8.33201	p	p
0.0777000	8.34435	8.34349	p	p

procedure here is as described in Ref. [1]: for a suitable range of fixed values of  $Z$  we automatically minimize the total ETF energy per nucleon,

$$e^{\text{ETF}} = e_{\text{Sky}}^{\text{ETF}} + e_C + e_e - Y_p Q_{n,\beta}, \quad (13)$$

with respect to six geometric variables and  $A$ . The complete results of these computations will be found in the Supplemental Material [30].

For each value of the mean density  $\bar{n}$  the optimal value of  $Z$  is then picked out by inspection, and the corresponding values of  $e^{\text{ETF}}$  are shown in columns 2 and 3 of Table I for cylindrical and plate shapes, respectively (the equilibrium values of  $Z$  are shown in Table VI). Reliable pasta solutions could not be found outside the range of densities shown. Referring to our complete numerical results presented in the Supplemental Material [30], it will be seen that at high densities close to the interface with the homogeneous core there are values of  $Z$  for which the calculated energy is significantly lower

than the value we have selected. These cases, which are easily recognized, are associated with very low values of the geometrical parameter  $C_q$ , which imply very steep density gradients, and thus a failure of the ETF expansion to converge.

Columns 4 and 5 of Table I show respectively the optimum ETF and ETFSI+BCS values of the energy per nucleon assuming a spherical configuration (see the Supplemental Material [30]). In this table the latter are all lower than the former, i.e., the shell and pairing corrections are all negative here, but this is not a general feature. For  $\bar{n} \gtrsim 0.073 \text{ fm}^{-3}$ , proton drip for spherical cells occurs [1], and we assume in our model that the shell and pairing corrections vanish [1]. Beyond  $\bar{n} = 0.0749994 \text{ fm}^{-3}$  the spherical solutions become mechanically unstable, with increasing mean density leading occasionally to reduced pressure. Note that below proton drip the optimal values of  $Z$  are different for ETF and ETFSI+BCS.

Using the method of Ducoin *et al.* [40], we showed in Ref. [1] that the transition to a homogeneous solution should occur at  $\bar{n} = 0.0807555 \text{ fm}^{-3}$  for the BSk24 functional. The fact that we can obtain no reliable solution either of pasta or spherical form when  $\bar{n} > 0.0777 \text{ fm}^{-3}$  suggests that there is a narrow range of densities that our codes cannot explore. In any case, the calculations of Ref. [40], being based on the Thomas-Fermi approximation considering small sinusoidal density fluctuations, do not necessarily yield the exact transition density.

#### A. Phase transitions and the equation of state

Comparing columns 2 and 3 of Table I with each of columns 4 and 5 determines the energetically preferred shape at each density, which we indicate by s (spherical), c (cylindrical), or p (plate). In the pasta phases the ETF values of the energy per nucleon differ at most by 0.05% from the values determined for spherical cells, which means that the analytic fit (C1) given in Ref. [1] will remain valid even when we allow the WS cells to be nonspherical.

We recall that the fit in Ref. [1] was designed to be used in a uniform manner throughout the entire neutron star, from its outer crust to the core. Then the accuracy within  $\approx 1\%$  of that fit was sufficient for this purpose. However, it would not allow us to study the *differences* between the energies in the three different phases. For this purpose we have constructed separate, more accurate fits for each phase, applicable in a restricted density range, specifically around the expected densities of the mantle,  $0.05 \text{ fm}^{-3} \lesssim \bar{n} < n_{cc}$ . For the energy per baryon  $e$ , this fit reads

$$e = a_1 + a_2x + \frac{a_3x}{(1 + a_4x)^3}, \quad (14)$$

where  $x \equiv \bar{n}/n_{cc}$  is the natural dimensionless density argument in the mantle, and the coefficients  $a_i$  are listed in Table II.

In Fig. 1 we show the calculated energy per baryon as a function of the mean baryon density and the fits. As noted above, the differences between the different cell shapes are almost indistinguishable, which means that the energy density is very weakly sensitive to the assumed WS cell shape. This makes the phase transitions sensitive to small corrections to the energy, depending on the theoretical model (such as ETF

TABLE II. Parameters of Eq. (14) for different WS cell shapes; sphere(1) and sphere(2) denote ETF and ETFSI+BCS values for the spherical shape, respectively.

Cell shape	$a_1$ (MeV)	$a_2$ (MeV)	$a_3$ (MeV)	$a_4$
sphere(1)	1.76708	4.1198	14.026	0.75683
sphere(2)	1.42067	4.2803	16.124	0.79924
cylinder	1.57416	4.2769	15.413	0.80464
plate	2.27349	4.1331	12.655	0.82983

or ETFSI+BCS for the spherical cells, in our case). In order to make a choice between the phases, one should consider the differences between the energy values. These differences are visualized in Fig. 2 by showing the energy after subtraction of a common background function, which is chosen to be the fit (14) for the spherical WS cells in the ETF theory (the first row of Table II). We see that the cylindrical shape becomes energetically preferred, that is the “sphere  $\rightarrow$  cylinder” transition occurs, at  $\bar{n} \approx (0.050\text{--}0.051) \text{ fm}^{-3}$ . Within the ETFSI formalism, at higher densities  $\bar{n}$  the energy for the spheres increases less steeply than both for the cylinders and for the spheres in the ETF formalism, which is revealed in the increasingly steep descent of the ETFSI+BCS curve in Fig. 2. Eventually, at  $\bar{n} \approx 0.067 \text{ fm}^{-3}$  the ETFSI+BCS energy for the spheres again becomes lower than the ETF energy for the cylinders; that is, the back transition “cylinder  $\rightarrow$  sphere” occurs. Note that with the ETFSI+BCS method the

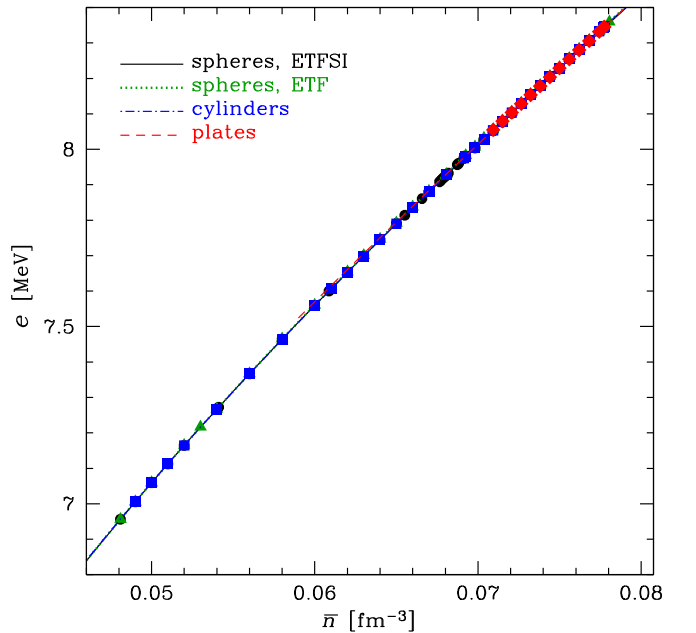


FIG. 1. Energy per baryon as function of the mean baryon density. Symbols show the calculated values and lines show the fit (14) for different WS cell shapes: spherical with shell and pairing corrections included (black dots and solid lines) or excluded (green triangles and dotted lines), cylindrical (blue squares and dot-dashed lines), and platelike (red diamonds and dashed lines).

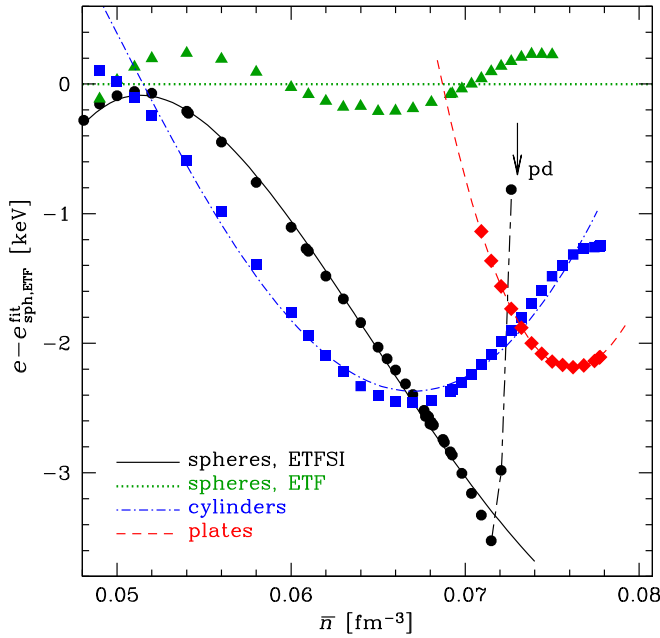


FIG. 2. The same as in Fig. 1, but, instead of energy  $e$ , the difference  $e - e_{\text{sph,ETF}}^{\text{fit}}$  is shown, where  $e_{\text{sph,ETF}}^{\text{fit}}$  is the fit (14) for the spherical WS cells in the ETF approximation. The long-dash-short-dash line connects the ETFSI+BCS results for the spheres at  $\bar{n} > 0.07207$ , where  $Z$  changes and the numerical results depart from the fit (14). The arrow, marked “pd,” points to the density of the proton drip in the spherical geometry according to Ref. [1].

number of protons per spherical WS cell is constant,  $Z = 40$ , for  $\bar{n} \lesssim 0.072 \text{ fm}^{-3}$  (see Ref. [1]), whereas the ETF method leads to noninteger continuously changing  $Z$ . The deviation of the ETFSI+BCS points beyond  $\bar{n} \gtrsim 0.072 \text{ fm}^{-3}$  in Fig. 2 (that are connected by a long-dash-short-dash line as a guide to the eye) is a consequence of the fact that  $Z$  is starting to change discontinuously for the ETFSI+BCS calculations at these densities. As a result, the second transition “sphere  $\rightarrow$  cylinder” occurs at  $\bar{n}$  between  $0.0720701$  and  $0.0726466 \text{ fm}^{-3}$ . It precedes the proton drip at  $\bar{n} \approx 0.073 \text{ fm}^{-3}$  [1] and the transition “cylinder  $\rightarrow$  plate,” which occurs at nearly the same density. In contrast, when we compare the ETF results for the spheres and the cylinders, we do not observe the back transition “cylinder  $\rightarrow$  sphere.”

Thus, for certain densities the preferred shape depends on whether we compare the ETF results for the cylinders and plates with the ETF or ETFSI+BCS results for the spheres, i.e., whether we exclude or include the shell and pairing corrections for the spherical configuration. While comparison with the ETF results yields the usual sequence of shapes with increasing density, “sphere  $\rightarrow$  cylinder  $\rightarrow$  plate,” over a certain density range comparison with the ETFSI+BCS results (shell and pairing corrections included) leads to the more complicated sequence of “sphere  $\rightarrow$  cylinder  $\rightarrow$  sphere  $\rightarrow$  cylinder  $\rightarrow$  plate.” Whether or not this rather unusual feature of a back transition “cylinder  $\rightarrow$  sphere” would survive the inclusion of the shell and pairing corrections to the pasta calculations depends very much on their magnitude: an inspection of Table I shows they would have to exceed 30% of

the corrections to the spherical ETF calculations for the back transition to be completely eliminated.

The density of the initial sphere  $\rightarrow$  cylinder transition is also seen to be *slightly* sensitive to whether we compare with columns 4 or 5: including the shell and pairing corrections for the spherical configuration shifts the transition density from  $\bar{n} = 0.050 \text{ fm}^{-3}$  to  $0.051 \text{ fm}^{-3}$ . But regardless of which option is chosen there is a disagreement with the calculations of Martin and Urban using the same method as described in Ref. [28]; they find that the sphere  $\rightarrow$  cylinder transition occurs at a density  $\bar{n} \simeq 0.057 \text{ fm}^{-3}$  for BSk24 [41]. Besides, they predict that the final cylinder  $\rightarrow$  plate transition occurs at a lower density, at about  $0.069 \text{ fm}^{-3}$ , compared to our estimate of  $0.073 \text{ fm}^{-3}$ .

In neither the spherical nor the nonspherical configurations do we find at beta equilibrium, i.e., for the equilibrating value of  $Z$ , any of the “inverted” solutions that were found in the original liquid-drop calculations of Ref. [23]. In this respect we agree with the ETF calculations of Martin and Urban using the same BSk24 functional [41].

For cylinders, proton drip starts for  $\bar{n}$  around  $0.077 \text{ fm}^{-3}$ , a density at which plates are energetically favored. And since for plates we nowhere find reliable solutions with proton drip, it follows that once we allow pasta shapes for the WS cells, proton drip can occur nowhere in the inner crust, except perhaps very close to the interface with the core.

Columns 2 and 3 of Table III show respectively the pressure (calculated as described in Appendix B of Ref. [15]) for the optimal ETF and ETFSI+BCS spherical configurations, while column 4 shows the pressure for the actual equilibrium shape: spherical (s), cylinder (c), or plate (p), as the case may be. In the pasta phases the pressure differs at most by 0.6% from the spherical-cell value, which means that the analytic fit (C4) of Ref. [1] is still applicable. Nevertheless, exactly as for the energy per baryon, we have constructed separate, more accurate fits for each phase, applicable in the restricted density range around the expected densities of the mantle. They read

$$P = a_1 + a_2x + \frac{a_3x^8}{1 + a_4x^{12}}, \quad (15)$$

where, as before,  $x \equiv \bar{n}/n_{\text{cc}}$ , and the coefficients  $a_i$  are listed in Table IV. Whereas the fit presented in Ref. [1] uniformly covers the entire neutron star and ensures the accuracy within 4%, the fit (15) is applicable only at  $0.05 \lesssim \bar{n} \lesssim 0.08 \text{ fm}^{-3}$ , but provides an accuracy within 0.1% with respect to the numerical data in Table III.

In Fig. 3 we show the pressure as function of the mean baryon density. We see that the pressure values for the different phases are almost indistinguishable, yet one can discern small differences in the slope: the EoS becomes stiffer along the transition sequence “sphere  $\rightarrow$  cylinder  $\rightarrow$  plate.”

In the gravitational field of a neutron star, one needs to know the chemical potentials of the different particles to determine the chemical equilibrium. The chemical potential of the strongly degenerate electrons  $\mu_e$  is determined by the formulas given in Appendix B of Ref. [1]. The chemical potential of protons is related to  $\mu_e$  and to the chemical potential of neutrons  $\mu_n$  by the condition of beta equilibrium,  $\mu_p = \mu_n - \mu_e$ , where  $\mu_n = g$ , the Gibbs free energy per

TABLE III. Pressure (in  $\text{MeV fm}^{-3}$ ). Columns 2 and 3 refer to spherical cells, without and with shell and pairing corrections, respectively. Column 4 refers to the equilibrium cell shape: s (spherical), c (cylindrical), and p (platelike).

$\bar{n}$	$P_{\text{sph}}(1)$	$P_{\text{sph}}(2)$	$P_{\text{eq}}$
0.0490000	0.1330	0.1330	0.1330 s
0.0500000	0.1364	0.1363	0.1357 c, 0.1363 s
0.0510000	0.1398	0.1398	0.1393 c
0.0520000	0.1433	0.1433	0.1427 c
0.0540000	0.1505	0.1505	0.1499 c
0.0560000	0.1580	0.1581	0.1573 c
0.0580000	0.1658	0.1659	0.1651 c
0.0600000	0.1739	0.1741	0.1733 c
0.0610000	0.1781	0.1783	0.1775 c
0.0620000	0.1824	0.1826	0.1817 c
0.0630000	0.1868	0.1870	0.1861 c
0.0640000	0.1913	0.1915	0.1906 c
0.0650000	0.1958	0.1962	0.1952 c
0.0660000	0.2005	0.2009	0.1999 c
0.0670000	0.2053	0.2057	0.2048 c
0.0680624	0.2105	0.2110	0.2101 c, 0.2110 s
0.0691445	0.2158	0.2164	0.2155 c, 0.2164 s
0.0692552	0.2164	0.2169	0.2160 c, 0.2169 s
0.0698092	0.2192	0.2198	0.2189 c, 0.2198 s
0.0703677	0.2220	0.2226	0.2218 c, 0.2226 s
0.0709307	0.2249	0.2255	0.2247 c, 0.2255 s
0.0714981	0.2279	0.2284	0.2277 c, 0.2284 s
0.0720701	0.2309	0.2313	0.2308 c, 0.2313 s
0.0726466	0.2338	0.2338	0.2339 c
0.0732278	0.2368	0.2368	0.2356 p
0.0738136	0.2399	0.2399	0.2390 p
0.0744042	0.2429	0.2429	0.2424 p
0.0749994	0.2459	0.2459	0.2458 p
0.0755994			0.2493 p
0.0762042			0.2528 p
0.0768139			0.2565 p
0.0774283			0.2601 p
0.0777000			0.2616 p

nucleon. For the chemical potential of neutrons, the fit (C18) of Ref. [1], originally constructed for the crust, holds also in the mantle, because the differences between  $\mu_n$  in the different phases lie within its accuracy level. However, for a study of phase equilibrium one needs to know the differences between  $\mu_n$  in the three phases. For this purpose we have constructed

TABLE IV. Parameters of Eq. (15) for different WS cell shapes; sphere(1) and sphere(2) denote ETF and ETFSI+BCS values for the spherical shape, respectively.

Cell shape	$a_1$ ( $\text{MeV fm}^{-3}$ )	$a_2$ ( $\text{MeV fm}^{-3}$ )	$a_3$ ( $\text{MeV fm}^{-3}$ )	$a_4$
sphere(1)	-0.01429	0.2399	0.1058	1.41
sphere(2)	-0.02128	0.25153	0.0934	1.35
cylinder	-0.02705	0.26	0.0785	0.866
plate	-0.184	0.463	0	-

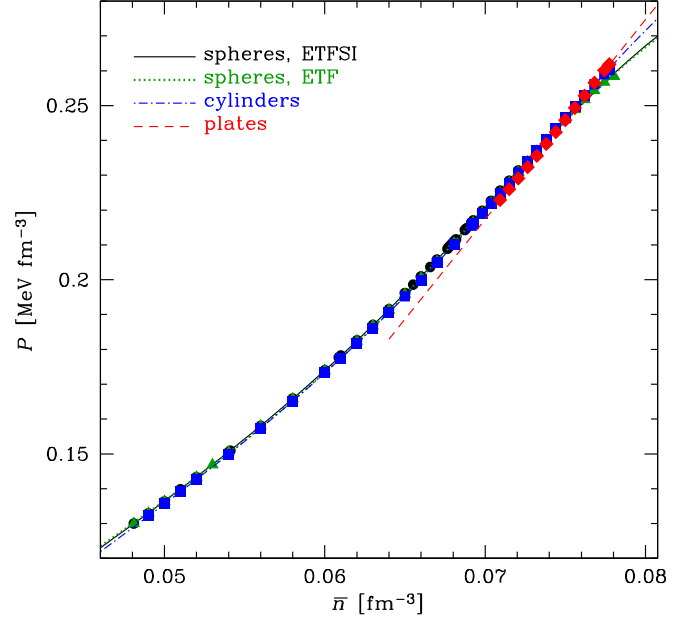


FIG. 3. Pressure as function of the mean baryon density. Symbols show the calculated values and lines show the fit (15) for different WS cell shapes: spherical with shell and pairing corrections included (black dots and solid lines) or excluded (green triangles and dotted lines), cylindrical (blue squares and dot-dashed lines), and platelike (red diamonds and dashed lines).

the following analytical approximations:

$$\mu_n - M_n c^2 = (a_1 + a_2 x + a_3 x^8)(a_4 - x)^{a_5}, \quad (16)$$

where  $x \equiv \bar{n}/n_{cc}$ , and the coefficients  $a_i$  are listed in Table V. As compared to the fit for  $\mu_n$  given by Eq. (C18) in Ref. [1], Eq. (16) has a narrow applicability range,  $0.05 \lesssim \bar{n} \lesssim 0.08 \text{ fm}^{-3}$  instead of  $2 \times 10^{-4} \lesssim \bar{n} \lesssim 0.08 \text{ fm}^{-3}$ , but in return it provides an order-of-magnitude better accuracy. The comparison of the calculated and fitted  $\mu_n$  is shown in Fig. 4. In the upper panel the differences between different results are barely distinguishable. In order to visualize them, in the lower panel we subtract from each  $\mu_n$  value the respective value given by the fitting formula (16) for the spherical WS cells in the ETF approximation (the first row of parameters in Table V). It is seen that in the vicinity of the transition densities the differences between the respective values of  $\mu_n$  are of the order of 10–20 keV.

TABLE V. Parameters of Eq. (16) for different WS cell shapes; sphere(1) and sphere(2) denote ETF and ETFSI+BCS values for the spherical shape, respectively.

Cell shape	$a_1$ (MeV)	$a_2$ (MeV)	$a_3$ (MeV)	$a_4$	$a_5$
sphere(1)	5.2813	9.2587	3.162	1.0677	0.15509
sphere(2)	5.2243	9.6969	4.358	1.0361	0.16681
cylinder	6.2911	6.0102	0.8103	1.0207	0.028241
plate	4.9556	10.0154	3.128	1.1295	0.20485

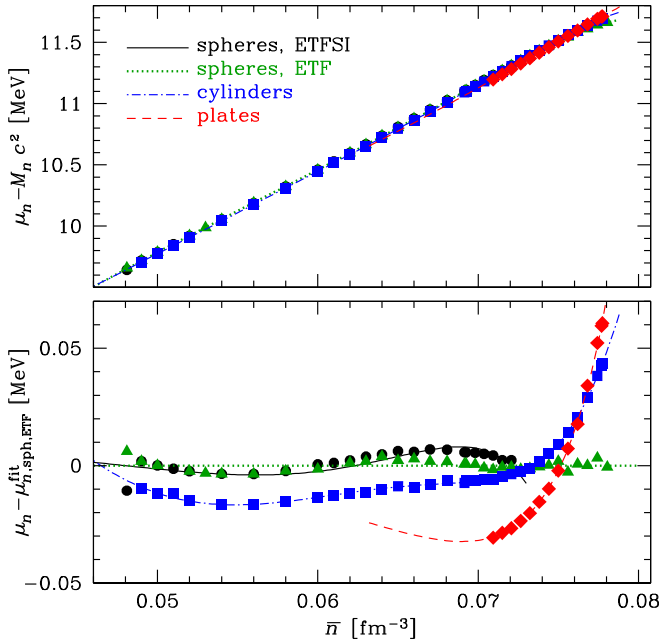


FIG. 4. Chemical potential of neutrons  $\mu_n$  as function of the mean baryon density. Symbols show the calculated values and lines show the fit (15) for different WS cell shapes: spherical with shell and pairing corrections included (black dots and solid lines) or excluded (green triangles and dotted lines), cylindrical (blue squares and dot-dashed lines), and platelike (red diamonds and dashed lines). *Upper panel*: the difference between  $\mu_n$  and the rest energy of neutron  $M_n c^2$ . *Lower panel*: the difference between  $\mu_n$  and the fit (16) to the ETF results for the spherical WS cells.

### B. Free and bound neutron and proton numbers

Column 2 of Table VI shows the equilibrium value of  $Z$ , regardless of shape. Since this quantity even has different dimensions for the different shapes (for spheres it is the number of protons in the cell, for cylinders the number per fm, and for plates the number per  $\text{fm}^2$ ) there can be no comparison of the pasta values with the spherical value. On the other hand, such a comparison is meaningful for the proton fraction  $Y_p = Z/A$ , so in columns 3 and 4 we display the values of  $Y_p$  assuming spherical cells, the first without shell and pairing corrections and the second with them. In column 5 we show the values of  $Y_p$  for the equilibrium pasta shape. Remarkably, despite the drastic difference in geometries almost the same values are obtained, the difference never exceeding 1%, which means that we can still use the analytic fit (C6) of Ref. [1]. Nevertheless, we have constructed separate, more accurate fits for each phase, applicable in the restricted density range, specifically around the expected densities of the mantle. It turns out that, in the considered density range,  $Y_p$  is well reproduced by the simple parabola

$$Y_p = Y_{\min} + a(\bar{n} - n_{\min})^2. \quad (17)$$

Here,  $\bar{n}$  is in units of  $\text{fm}^{-3}$  and the parameters are listed in Table VII. The comparison of calculated and fitted proton fractions is shown in Fig. 5.

TABLE VI. Proton number  $Z$  and fraction  $Y_p$ . Column 2 shows  $Z$  value for the actual equilibrium shape (note that units depend on shape). Columns 3 and 4 show  $Y_p$  for spherical cells, without and with shell and pairing corrections, respectively. Column 4 shows  $Y_p$  for the equilibrium cell shape: s (spherical), c (cylindrical), and p (platelike).

$\bar{n}$	$Z_{\text{eq}}$	$Y_p^{\text{sph}}(1)$	$Y_p^{\text{sph}}(2)$	$Y_p^{\text{eq}}$
0.0490000	40 s	0.03366	0.03358	0.03358 s
0.0500000	1.503 c, 40 s	0.03354	0.03346	0.03372 c, 0.03346 s
0.0510000	1.501 c	0.03344	0.03335	0.03369 c
0.0520000	1.490 c	0.03333	0.03325	0.03351 c
0.0540000	1.482 c	0.03317	0.03308	0.03333 c
0.0560000	1.476 c	0.03301	0.03292	0.03318 c
0.0580000	1.472 c	0.03289	0.03280	0.03306 c
0.0600000	1.472 c	0.03280	0.03270	0.03296 c
0.0610000	1.474 c	0.03277	0.03265	0.03292 c
0.0620000	1.476 c	0.03273	0.03262	0.03289 c
0.0630000	1.480 c	0.03272	0.03259	0.03287 c
0.0640000	1.484 c	0.03267	0.03257	0.03285 c
0.0650000	1.492 c	0.03270	0.03256	0.03284 c
0.0660000	1.528 c	0.03269	0.03255	0.03286 c
0.0670000	1.512 c	0.03271	0.03255	0.03284 c
0.0680624	1.528 c, 40 s	0.03271	0.03256	0.03297 c, 0.03256 s
0.0691445	1.542 c, 40 s	0.03274	0.03257	0.03287 c, 0.03257 s
0.0692552	1.546 c, 40 s	0.03274	0.03258	0.03287 c, 0.03258 s
0.0698092	1.554 c, 40 s	0.03275	0.03259	0.03288 c, 0.03259 s
0.0703677	1.566 c, 40 s	0.03278	0.03260	0.03290 c, 0.03260 s
0.0709307	1.576 c, 40 s	0.03279	0.03262	0.03291 c, 0.03262 s
0.0714981	1.590 c, 40 s	0.03281	0.03264	0.03293 c, 0.03264 s
0.0720701	1.604 c, 41 s	0.03282	0.03267	0.03295 c, 0.03267 s
0.0726466	1.618 c	0.03285	0.03296	0.03297 c
0.0732278	0.0643 p	0.03288	0.03288	0.03316 p
0.0738136	0.0643 p	0.03290	0.03290	0.03318 p
0.0744042	0.0643 p	0.03293	0.03294	0.03320 p
0.0749994	0.0646 p	0.03296	0.03296	0.03324 p
0.0755994	0.0642 p			0.03337 p
0.0762042	0.0649 p			0.03342 p
0.0768138	0.0652 p			0.03333 p
0.0774283	0.0657 p			0.03337 p
0.0777000	0.0673 p			0.03342 p

In practice, for modeling physical processes in the neutron-star crust and mantle and determining their physical properties, one needs to know not only  $Y_p$ , but also the numbers of free and bound neutrons and protons in a WS cell. For this purpose we have constructed appropriate fitting formulas.

TABLE VII. Parameters of Eq. (17) for different WS cell shapes; sphere(1) and sphere(2) denote ETF and ETFSI+BCS values for the spherical shape, respectively.

Cell shape	$Y_{\min}$	$a$ ( $\text{fm}^6$ )	$n_{\min}$ ( $\text{fm}^{-3}$ )
sphere(1)	0.03267	3.56	0.0660
sphere(2)	0.03255	3.54	0.0663
cylinder	0.03284	3.17	0.0663
plate	0.03301	3.17	0.0663

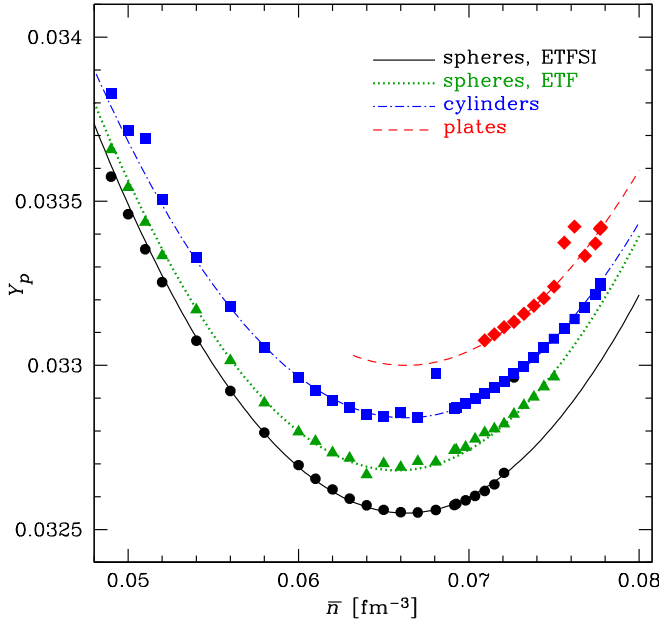


FIG. 5. Proton fraction as function of the mean baryon density. Symbols show the calculated values and lines show the fit (17) for different WS cell shapes: spherical with shell and pairing corrections included (black dots and solid lines) or excluded (green triangles and dotted lines), cylindrical (blue squares and dot-dashed lines), and platelike (red diamonds and dashed lines).

For the spherical WS cells such fits are given in section C3.1 of Ref. [1]; they remain unchanged. For the total number of protons in the cylindrical WS cells we have, with an accuracy of a few percent,

$$Z = (1.835 - 0.554x + 0.732x^9) \text{ fm}^{-1}, \quad (18)$$

where  $x = \bar{n}/n_{cc}$ . For platelike cells, at  $\bar{n} < 0.074 \text{ fm}^{-3}$  the proton number is constant,  $Z \approx Z_0$ , where  $Z_0 = 0.0643 \text{ fm}^{-2}$ . At  $\bar{n} > 0.074 \text{ fm}^{-3}$ ,  $Z$  increases approximately as  $Z/Z_0 \approx 1 + (11\Delta\bar{n})^4$ , where  $\Delta\bar{n} = \bar{n}/\text{fm}^{-3} - 0.074$ . The number of neutrons  $N$  is determined by the identity

$$N = Z \left( \frac{1}{Y_p} - 1 \right). \quad (19)$$

The numbers of unbound neutrons and protons are defined as  $N_{\text{free}} = n_{Bn}V_{\text{cell}}$  and  $Z_{\text{free}} = n_{Bp}V_{\text{cell}}$ , where  $V_{\text{cell}} = 4\pi R^3/3$ ,  $\pi R^2$ , and  $2R$  for the spheres, cylinders, and plates, respectively (accordingly, the numbers of free nucleons are counted per unit length for the cylinders and per unit area for the plates). The numbers of the neutrons and protons that are bound in clusters are  $N_{\text{cl}} = N - N_{\text{free}}$  and  $Z_{\text{cl}} = Z - Z_{\text{free}}$ . The numbers of free protons in the cylindrical and platelike WS cells are described by the fit

$$Z_{\text{free}} = \frac{(a_1x)^9}{(a_2 - x)^{a_3}}, \quad (20)$$

where  $Z_{\text{free}}$  is in  $\text{fm}^{-1}$  and  $\text{fm}^{-2}$  for the cylinders and plates, respectively,  $x \equiv \bar{n}/n_{cc}$ , and the parameters  $a_i$  are given in Table VIII. The fraction of free neutrons among all nucleons

TABLE VIII. Parameters of Eq. (20) for the cylindrical and platelike WS cells.

Cell shape	$a_1$	$a_2$	$a_3$
cylinder	0.62144	1.0133	1.2708
plate	0.26563	1.1712	4.5795

$Y_{nf} \equiv N_{\text{free}}/A$  is approximated as

$$Y_{nf} = a_1 + a_2x + a_3x^{a_4}, \quad x \equiv \bar{n}/n_{cc}, \quad (21)$$

with parameters given in Table IX. Now with  $Z$  and  $Y_p$  already parametrized, the number of free neutrons is given by the identity  $N_{\text{free}} = ZY_{nf}/Y_p$ .

The calculated and fitted total and bound proton numbers are shown in Figs. 6 and 7. Note that although the proton-drip threshold, as defined by Eq. (6), is not reached in any layer of the crust,  $Z_{\text{free}}$  becomes appreciable at densities  $\bar{n} \gtrsim 0.07 \text{ fm}^{-3}$ .

### C. Nuclear size and shape parameters

For studies of some physical phenomena in neutron star interiors, it may be of interest to know the sizes and shapes of the nuclear clusters (see, e.g., Ref. [42] for the case of electron heat and charge transport). For this purpose, we have constructed analytical approximations to the parameters  $C_q$  and  $a_q$ , which determine respectively the size and the diffuseness of a cluster, when its density profile is parametrized by Eqs. (4) and (5). For the spherical WS cells, the fits to  $C_q$  and  $a_q$  as functions of mean baryon density  $\bar{n}$  have been published in Appendix C5 of Ref. [1]; they remain unchanged. For the cylindrical and platelike WS cells, in the restricted ranges of  $\bar{n}$  under consideration, they are approximated by the simple formula

$$X_q = a_1 + a_2x^{a_3}, \quad X_q = C_p, C_n, a_p, a_n; \quad x \equiv \bar{n}/n_{cc}. \quad (22)$$

The fit parameters  $a_i$  are given in Table X. The calculated and fitted  $C_p$ ,  $C_n$ ,  $a_p$ , and  $a_n$  are plotted against  $\bar{n}$  in Fig. 8.

Note that we do not need separate fits to the parameters  $n_{Bq}$  and  $n_{\Lambda q}$  in Eq. (5), because they are determined by the already fitted parameters through the relations

$$n_{Bp} = \frac{Z_{\text{free}}}{V_{\text{cell}}}, \quad n_{Bn} = \frac{N_{\text{free}}}{V_{\text{cell}}}, \quad (23)$$

$$n_{\Lambda p} = \frac{Z_{\text{cl}}}{\int_0^R f_p(\xi) \frac{dV}{d\xi} d\xi}, \quad n_{\Lambda n} = \frac{N_{\text{cl}}}{\int_0^R f_n(\xi) \frac{dV}{d\xi} d\xi}, \quad (24)$$

TABLE IX. Parameters of Eq. (21) for the cylindrical and platelike WS cells.

Cell shape	$a_1$	$a_2$	$a_3$	$a_4$
cylinder	0.74483	0.0959	0.0817	26
plate	0.77675	0.0455	0.0446	21

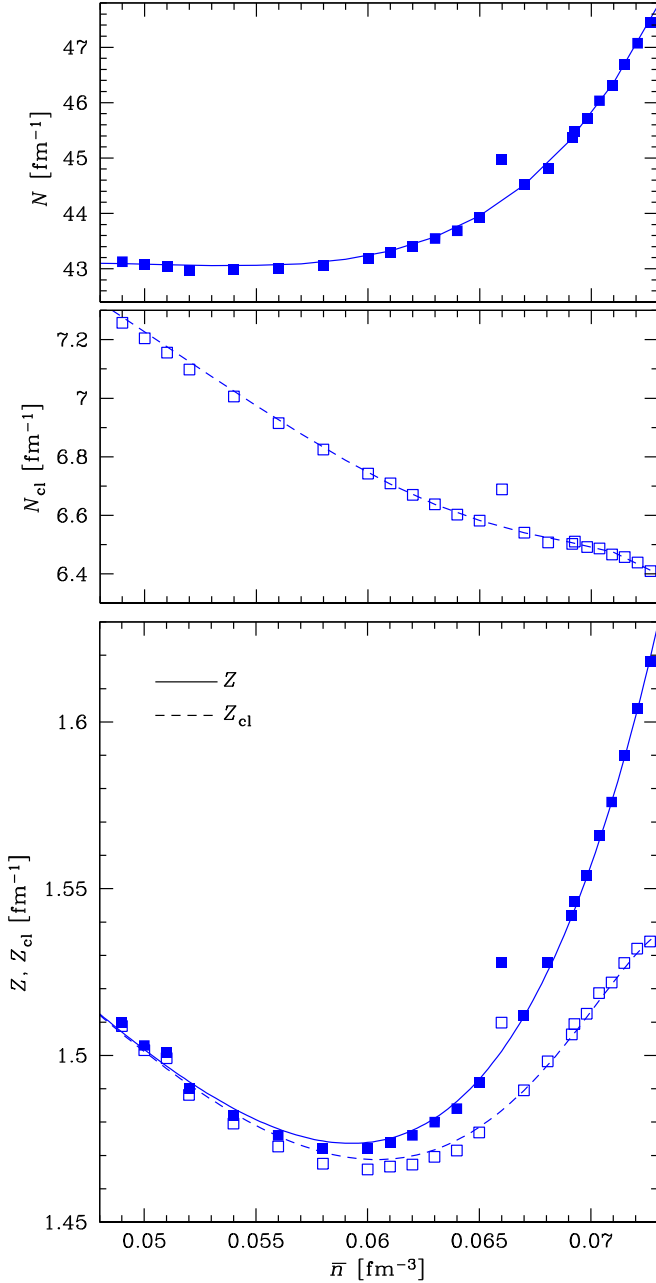


FIG. 6. Proton and neutron numbers per unit length as functions of mean baryon density of a cylindrical WS cell. *Top panel*: all neutrons; *middle panel*: clustered neutrons; *bottom panel*: all protons (filled symbols and solid lines) and clustered protons (empty symbols and dashed lines). The symbols show the calculated values and the lines show the fits.

where

$$\frac{dV}{d\xi} = \begin{cases} 4\pi r^2 & (\text{spheres}), \\ 2\pi\eta & (\text{cylinders}), \\ 2 & (\text{plates}). \end{cases}$$

#### D. Inhomogeneity

Regardless of the cell shape, a measure of the inhomogeneity of the inner crust is given by what we have called the

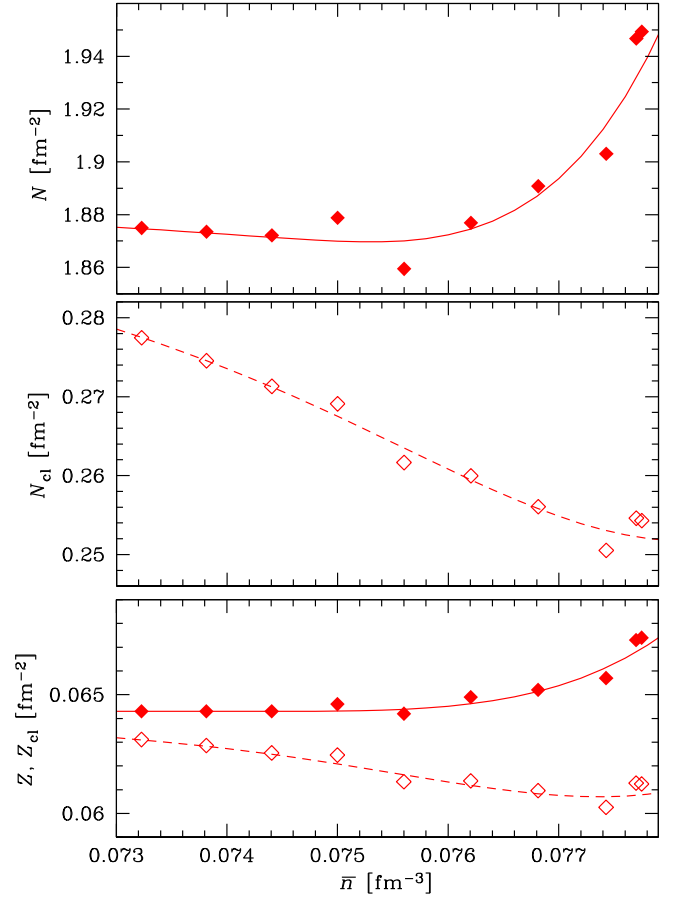


FIG. 7. Proton and neutron numbers per unit area as functions of mean baryon density of a platelike WS cell. *Top panel*: all neutrons; *middle panel*: clustered neutrons; *bottom panel*: all protons (filled symbols and solid lines) and clustered protons (empty symbols and dashed lines). The symbols show the calculated values and the lines show the fits.

inhomogeneity factor,

$$\Lambda = \frac{1}{V_{\text{cell}}} \int \left( \frac{n(\mathbf{r})}{\bar{n}} - 1 \right)^2 d^3\mathbf{r}, \quad (25)$$

where  $V_{\text{cell}}$  is the cell volume. Of particular interest from the standpoint of transport properties is the analogous quantity

TABLE X. Parameters of Eq. (22) for the cylindrical and platelike WS cells. Parameters  $a_1$  and  $a_2$  are in units of fm,  $a_3$  is dimensionless.

Parameter	Shape					
	Cylinder			Plate		
	$a_1$	$a_2$	$a_3$	$a_1$	$a_2$	$a_3$
$C_p$	5.35	5.24	6.83	4.191	4.30	16
$C_n$	5.97	4.73	6.53	4.799	3.82	16
$a_p$	0.729	1.55	6.12	0.7553	0.793	10
$a_n$	1.214	1.37	5.09	0.9027	0.578	10

TABLE XI. Inhomogeneities  $\Lambda$  and  $\Lambda_p$ , defined in Eqs. (25) and (26), respectively. Columns 2 and 3 show  $\Lambda$  for spherical cells, without and with shell and pairing corrections, respectively; columns 5 and 6 the corresponding values of  $\Lambda_p$ . Columns 4 and 7 show  $\Lambda$  and  $\Lambda_p$ , respectively, for the actual equilibrium shape.

$\bar{n}$	$\Lambda^{\text{sph}}(1)$	$\Lambda^{\text{sph}}(2)$	$\Lambda^{\text{eq}}$	$\Lambda_p^{\text{sph}}(1)$	$\Lambda_p^{\text{sph}}(2)$	$\Lambda_p^{\text{eq}}$
0.0490000	0.170	0.169	0.169 s	6.39	6.45	6.45 s
0.0500000	0.162	0.161	0.162 c 0.161 s	6.11	6.17	5.92 c 6.17 s
0.0510000	0.154	0.153	0.154 c	5.84	5.90	5.66 c
0.0520000	0.146	0.145	0.146 c	5.58	5.63	5.41 c
0.0540000	0.131	0.130	0.132 c	5.07	5.13	4.93 c
0.0560000	0.118	0.117	0.118 c	4.60	4.66	4.48 c
0.0580000	0.105	0.105	0.106 c	4.16	4.22	4.05 c
0.0600000	0.0939	0.0932	0.0942 c	3.74	3.80	3.65 c
0.0610000	0.0885	0.0878	0.0888 c	3.53	3.60	3.45 c
0.0620000	0.0833	0.0825	0.0836 c	3.34	3.41	3.27 c
0.0630000	0.0782	0.0775	0.0785 c	3.14	3.22	3.08 c
0.0640000	0.0731	0.0726	0.0737 c	2.98	3.03	2.90 c
0.0650000	0.0686	0.0678	0.0690 c	2.76	2.85	2.73 c
0.0660000	0.0639	0.0632	0.0645 c	2.59	2.67	2.55 c
0.0670000	0.0595	0.0587	0.0600 c	2.41	2.50	2.39 c
0.0680624	0.0547	0.0540	0.0554 c, 0.0540 s	2.23	2.31	2.20 c, 2.31 s
0.0691445	0.0501	0.0493	0.0508 c, 0.0493 s	2.03	2.13	2.03 c, 2.13 s
0.0692552	0.0496	0.0489	0.0504 c, 0.0489 s	2.01	2.11	2.01 c, 2.11 s
0.0698092	0.0472	0.0465	0.0481 c, 0.0465 s	1.92	2.01	1.93 c, 2.01 s
0.0703677	0.0449	0.0441	0.0458 c, 0.0441 s	1.82	1.91	1.84 c, 1.91 s
0.0709307	0.0425	0.0417	0.0435 c, 0.0417 s	1.73	1.82	1.75 c, 1.82 s
0.0714981	0.0401	0.0392	0.0412 c, 0.0392 s	1.64	1.72	1.66 c, 1.72 s
0.0720701	0.0377	0.0369	0.0389 c, 0.0369 s	1.54	1.61	1.57 c, 1.61 s
0.0726466	0.0353	0.0353	0.0366 c	1.44	1.44	1.48 c
0.0732278	0.0328	0.0328	0.0327 p	1.34	1.34	1.16 p
0.0738136	0.0303	0.0303	0.0306 p	1.24	1.24	1.09 p
0.0744042	0.0277	0.0277	0.0285 p	1.14	1.14	1.02 p
0.0749994	0.0250	0.0250	0.0265 p	1.03	1.03	0.950 p
0.0755994			0.0243 p			0.874 p
0.0762042			0.0222 p			0.801 p
0.0768138			0.0200 p			0.730 p
0.0774283			0.0177 p			0.652 p
0.0777000			0.0168 p			0.613 p

defined entirely in terms of the proton distribution,

$$\Lambda_p = \frac{1}{V_{\text{cell}}} \int \left( \frac{n_p(\mathbf{r})}{\bar{n}_p} - 1 \right)^2 d^3\mathbf{r}, \quad (26)$$

where  $\bar{n}_p = Y_p \bar{n}$ .

Columns 2 and 3 of Table XI show respectively the values of  $\Lambda$  for the optimal ETF and ETFSI+BCS spherical configurations, while column 4 shows the values of  $\Lambda$  for the actual equilibrium shape: spherical (s), cylinder (c) or plate (p), as the case may be. In columns 5, 6, and 7 we display the comparable quantities for  $\Lambda_p$ . The difference in the value of  $\Lambda$  between spherical and pasta shapes never exceeds 6%, but for  $\Lambda_p$  the difference can amount to 15%. Thus in this respect imposing the constraint of a spherical cell shape can do no more than provide a qualitative guide as to what happens when pasta shapes are allowed. Nevertheless, it is perhaps remarkable that even this level of similarity exists, given the quite different cell shapes that are being compared.

Inhomogeneities can be alternatively characterized in terms of the volume fraction occupied by clusters. This quantity is of particular interest since, in the liquid-drop picture, spherical clusters are predicted to become unstable against quadrupole deformations when their filling fraction exceeds  $1/8 = 12.5\%$  [22]. Then spaghetti configurations become stable in place of spherical ones. At a filling fraction of  $1/2$  clusters are predicted to “turn inside out” [43]. On the other hand, quantum-molecular dynamics simulations [44] indicated that clusters remain quasispherical until they touch, similarly to percolating networks, as speculated earlier by Ogasawara and Sato [45]. According to these simulations, the onset of pasta formation is essentially determined by the maximum packing fraction of spherical clusters, which is given by  $\sqrt{3}\pi/8 \simeq 68.0\%$  for a body-centered cubic lattice. To compare with these predictions, we have estimated the filling fraction of spherical clusters. A natural definition is to take  $(C_q/R)^3$ , depending on whether clusters are characterized by the proton or neutron distributions (the definition can be easily extended to cylinders and plates, the exponent 3 being

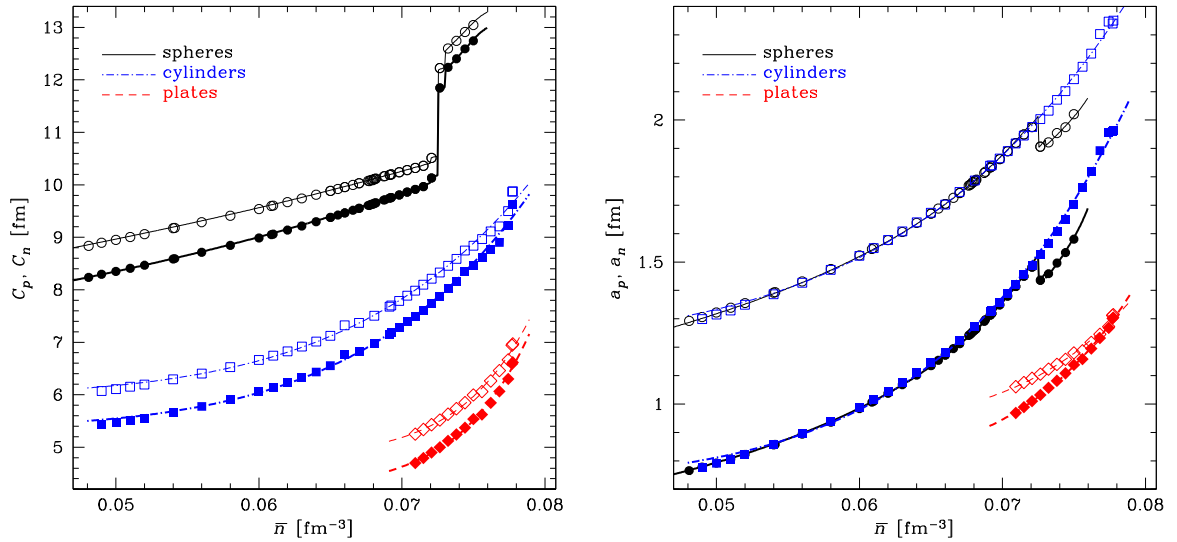


FIG. 8. Proton (filled symbols) and neutron (empty symbols) size parameters  $C_q$  (left panel) and diffuseness parameters  $a_q$  (right panel) compared to the fits (22) (lines) as functions of mean baryon density for different WS cell shapes: spherical (black dots and solid lines), cylindrical (blue squares and dot-dashed lines), and platelike (red diamonds and dashed lines).

replaced by 2 and 1, respectively). However, this definition is insensitive to the diffusivity coefficients  $a_q$  of the nucleon distributions. As an alternative definition we therefore assume that the nucleons characterizing the clusters are uniformly distributed, as in the liquid-drop picture, and define the filling fraction in terms of the ratio

$$\frac{V_{\text{cl}}}{V} = \frac{A_{\text{cl}}}{A} \frac{\bar{n}}{n_{\Lambda,p} + n_{\Lambda,n}}, \quad (27)$$

with

$$A_{\text{cl}} = 4\pi \int_0^R r^2 [f_n(r)n_{\Lambda,n} + f_p(r)n_{\Lambda,p}] dr \quad (28)$$

determining the number of nucleons contained in a single cluster. These different definitions of the filling fraction lead to remarkably similar numerical values. More importantly, the threshold value of the filling fraction above which spherical cells become unstable against pasta formation turns out to be in close agreement with the liquid-drop criterion, as can be seen in Table XII. Likewise, inspection of Table XIII shows that the transition from cylinders to plates occurs for a volume fraction  $\approx 31\%$ , comparable to that obtained by Hashimoto *et al.* [24]. Moreover, the absence of inverted configurations from our solutions could have been anticipated from the fact that the filling fraction never exceeds 55% (see Table XIV); cylindrical tubes or spherical bubbles are only predicted at

filling fractions above  $\approx 65\%$ . However, the back transition cylinder  $\rightarrow$  sphere is not found in liquid-drop models.

The disagreement of the quantum-molecular dynamics simulations with our calculations may stem from the fact that the former were carried out at finite temperatures and for a fixed proton fraction  $Y_p \approx 0.39$ , which is much higher than expected in the mantle of neutron stars.

#### IV. CONCLUDING REMARKS

Using the nuclear density functional BSk24, we have generalized our neutron-star calculations of Ref. [1] to include the possibility of pasta shapes for the WS cells of the inner crust, the earlier calculations having been confined to spherical cells. The spherical calculations used the ETF method with shell and pairing corrections added, but in the present pasta calculations neither of these corrections was made. Thus in comparing our pasta and spherical-cell results we take two different forms for the latter. First, we compare our pasta results with the pure ETF spherical-cell results, i.e., without the corrections, and find with increasing density the sequence sphere  $\rightarrow$  cylinder  $\rightarrow$  plate of cell shapes before the transition to the homogeneous core. We do not find any “inverted,” i.e., bubblelike, configurations, although we cannot exclude their existence in a narrow band of densities immediately below the crust-core transition. The filling fractions associated with

TABLE XII. Filling fractions for spherical clusters from ETFSI+BCS (ETF) calculations.

$\bar{n}$	$(C_n/R)^3$	$(C_p/R)^3$	$V_{\text{cl}}/V$
0.049000	0.121339 (0.123286)	0.098333 (0.100585)	0.124656 (0.126328)
0.050000	0.125640 (0.127702)	0.102046 (0.104407)	0.128922 (0.130704)
0.051000	0.130075 (0.132241)	0.105898 (0.108365)	0.133306 (0.135192)
0.052000	0.134665 (0.136946)	0.109902 (0.112491)	0.137826 (0.139832)
0.054000	0.144367 (0.147488)	0.118443 (0.121963)	0.147344 (0.150129)

TABLE XIII. Filling fractions for cylinders from ETF calculations.

$\bar{n}$	$(C_n/R)^2$	$(C_p/R)^2$	$V_{cl}/V$
0.049000	0.127064	0.101491	0.128928
0.050000	0.131514	0.105288	0.133315
0.051000	0.136202	0.109334	0.137894
0.052000	0.140894	0.113343	0.142514
0.054000	0.151083	0.122233	0.152432
0.056000	0.162127	0.131998	0.163108
0.058000	0.174214	0.142831	0.174701
0.060000	0.187513	0.154930	0.187341
0.061000	0.194750	0.161616	0.194177
0.062000	0.202324	0.168647	0.201292
0.063000	0.210379	0.176160	0.208812
0.064000	0.218882	0.184203	0.216719
0.065000	0.228075	0.192952	0.225217
0.066000	0.239043	0.203723	0.235369
0.067000	0.248148	0.212451	0.243640
0.068062	0.260073	0.224208	0.254482
0.069144	0.272906	0.237092	0.266115
0.069255	0.274510	0.238616	0.267560
0.069809	0.281509	0.245700	0.273866
0.070368	0.289058	0.253392	0.280659
0.070931	0.296728	0.261202	0.287515
0.071498	0.305086	0.269872	0.295000
0.072070	0.313700	0.278948	0.302700
0.072647	0.322679	0.288414	0.310702
0.073228	0.332248	0.298555	0.319211

the phase changes that we find are in remarkable agreement with predictions based on liquid-drop considerations, as is the absence of “inverted” solutions.

Given that there are indications that the corrections to the ETF pasta calculations might be significantly smaller than for spherical WS cells, it is of interest to compare our pasta results with those of the full spherical calculations, i.e., with the corrections to the latter included. The most significant change that emerges on making this comparison is a more complex sequence of cell shapes: sphere  $\rightarrow$  cylinder  $\rightarrow$  sphere  $\rightarrow$  cylinder  $\rightarrow$  plate. This new feature of a “back transition”

TABLE XIV. Filling fractions for plates from ETF calculations.

$\bar{n}$	$C_n/R$	$C_p/R$	$V_{cl}/V$
0.070931	0.383118	0.342791	0.369547
0.071498	0.392846	0.352870	0.378884
0.072070	0.403015	0.363550	0.388662
0.072647	0.413754	0.374796	0.398942
0.073228	0.425104	0.386800	0.409820
0.073814	0.436886	0.399368	0.421095
0.074404	0.449399	0.412764	0.433053
0.074999	0.462759	0.427263	0.445855
0.075599	0.476290	0.441886	0.458714
0.076204	0.491549	0.458818	0.473379
0.076814	0.507352	0.476426	0.488523
0.077428	0.524407	0.495647	0.504909
0.077700	0.535655	0.508414	0.515874

would be completely eliminated only if the neglected corrections in our pasta calculations amounted to more than 30% of the correction terms in the spherical-cell calculations. However, to be absolutely certain on this point it would be necessary to perform full ETFSI+BCS calculations of pasta.

While there is a certain narrow band of densities in the inner crust in which we cannot be sure whether the shape of the WS cell should be cylindrical or spherical, perhaps the most significant conclusion to be drawn from the present calculations is that in many respects the precise cell shape is irrelevant. In particular, we find that to a very good approximation the EoS and the proton fraction  $Y_p$  are the same whether we assume spherical, cylindrical, or platelike shapes for the WS cells. Thus the global fitting formulas developed in Ref. [1] for spherical cells remain valid here to the same level of accuracy as before. Here, over the restricted density range  $0.05 \text{ fm}^{-3} \lesssim \bar{n} < n_{cc}$ , we have constructed for each of the three phase states more accurate fits that well represent the small differences between the different phases.

The very small energy differences that we find between the different cell shapes are to be contrasted with the much larger differences found in the very recent calculations of Schuetrumpf *et al.* [46]. However, their calculations were performed at fixed values of the proton fraction  $Y_p$  much larger than the equilibrium values that we have found here.

Our results are to some extent dependent on the exact form of the parametrization (5) that we have chosen for the density distributions. The ideal solution would be to solve the Euler-Lagrange equations, but this is computationally impractical in a large-scale investigation of the scope that we have undertaken here.

## ACKNOWLEDGMENTS

We thank A. K. Dutta for his contributions to early developments of the code, and are grateful to Noel Martin for private communications. The work of J.M.P. was supported by NSERC (Canada) and the Fonds de la Recherche Scientifique (Belgium) under Grant No. CDR-J.0115.18. J.M.P. was also partially funded by the Université Libre de Bruxelles as a “Chaire internationale” during the tenure of which the present work was completed. The work of N.C. was supported by Fonds de la Recherche Scientifique (Belgium) under Grants No. CDR-J.0115.18 and No. IISN 4.4502.19. The work of A.Y.P. was supported by the Russian Science Foundation under Grant No. 19-12-00133.

## APPENDIX: CALCULATION OF COULOMB ENERGY

To derive Eqs. (7), (9), and (11) we begin with the general expression for the total Coulomb energy of a charge distribution  $n_{ch}(\mathbf{r})$ ,

$$E_C = \frac{1}{2} e^2 \int n_{ch}(\mathbf{r}) V_C(\mathbf{r}) d^3\mathbf{r}, \quad (\text{A1})$$

where the Coulomb field  $V_C(\mathbf{r})$  satisfies Poisson’s equation,

$$\nabla^2 V_C(\mathbf{r}) = -4\pi n_{ch}(\mathbf{r}). \quad (\text{A2})$$

In our case the charge distribution satisfies the neutrality condition

$$\int n_{\text{ch}}(\mathbf{r})d^3\mathbf{r} = 0. \quad (\text{A3})$$

For spherical cells Eq. (A1) becomes

$$E_C = 2\pi e^2 \int_0^R n_{\text{ch}}(r)V_C(r)r^2 dr. \quad (\text{A4})$$

Integrating this by parts we have

$$E_C = -2\pi e^2 \int_0^R u(r)\frac{dV_C(r)}{dr} dr, \quad (\text{A5})$$

where  $u(r)$  is given by Eq. (8) and we have made use of the relations

$$u(r=0) = u(r=R) = 0, \quad (\text{A6})$$

the latter following from neutrality. But from Eq. (A2)

$$4\pi n_{\text{ch}}(r) = -\frac{1}{r^2} \frac{d}{dr} \left( r^2 \frac{dV_C(r)}{dr} \right), \quad (\text{A7})$$

whence

$$\frac{dV_C(r)}{dr} = -\frac{4\pi}{r^2} u(r). \quad (\text{A8})$$

Equation (7) follows at once.

For cylindrical cells Eq. (A1) becomes

$$E_C = \pi e^2 \int_0^R n_{\text{ch}}(\eta)V_C(\eta)\eta d\eta. \quad (\text{A9})$$

Integrating this by parts we have

$$E_C = -\pi e^2 \int_0^R u(\eta)\frac{dV_C(\eta)}{d\eta} d\eta, \quad (\text{A10})$$

where  $u(\eta)$  is given by Eq. (10) and we have made use of the relations

$$u(\eta=0) = u(\eta=R) = 0. \quad (\text{A11})$$

But from Eq. (A2)

$$4\pi n_{\text{ch}}(\eta) = -\frac{1}{\eta} \frac{d}{d\eta} \left( \eta \frac{dV_C(\eta)}{d\eta} \right), \quad (\text{A12})$$

whence

$$\frac{dV_C(\eta)}{d\eta} = -\frac{4\pi}{\eta} u(\eta). \quad (\text{A13})$$

Equation (9) follows at once.

For platelike cells Eq. (A1) becomes

$$E_C = e^2 \int_0^R n_{\text{ch}}(z)V_C(z)dz. \quad (\text{A14})$$

Integrating this by parts we have

$$E_C = -e^2 \int_0^R u(z)\frac{dV_C(z)}{dz} dz, \quad (\text{A15})$$

where  $u(z)$  is given by Eq. (12) and we have made use of the relations

$$u(z=0) = u(z=R) = 0. \quad (\text{A16})$$

But from Eq. (A2)

$$4\pi n_{\text{ch}}(z) = -\frac{d}{dz} \left( \frac{dV_C(z)}{dz} \right), \quad (\text{A17})$$

whence

$$\frac{dV_C(z)}{dz} = -4\pi u(z). \quad (\text{A18})$$

Equation (11) follows at once.

- 
- [1] J. M. Pearson, N. Chamel, A. Y. Potekhin, A. F. Fantina, C. Ducoin, A. K. Dutta, and S. Goriely, *Mon. Not. R. Astron. Soc.* **481**, 2944 (2018); **486**, 768 (2019).
- [2] F. Douchin and P. Haensel, *Astron. Astrophys.* **380**, 151 (2001).
- [3] P. Haensel and A. Y. Potekhin, *Astron. Astrophys.* **428**, 191 (2004).
- [4] P. Haensel, A. Y. Potekhin, and D. G. Yakovlev, *Neutron Stars I: Equation of State and Structure* (Springer, New York, 2007).
- [5] A. F. Fantina, N. Chamel, J. M. Pearson, and S. Goriely, *Astron. Astrophys.* **559**, A128 (2013).
- [6] A. Y. Potekhin, A. F. Fantina, N. Chamel, J. M. Pearson, and S. Goriely, *Astron. Astrophys.* **560**, A48 (2013).
- [7] M. Fortin, C. Providência, Ad. R. Raduta, F. Gulminelli, J. L. Zdunik, P. Haensel, and M. Bejger, *Phys. Rev. C* **94**, 035804 (2016).
- [8] S. Goriely, N. Chamel, and J. M. Pearson, *Phys. Rev. C* **88**, 024308 (2013).
- [9] N. Chamel, S. Goriely, and J. M. Pearson, *Phys. Rev. C* **80**, 065804 (2009).
- [10] N. Chamel, *Phys. Rev. C* **82**, 014313 (2010).
- [11] G. Audi, M. Wang, A. H. Wapstra, F. G. Kondev, M. MacCormick, X. Xu, and B. Pfeiffer, *Chin. Phys. C* **36**, 1287 (2012).
- [12] D. Blaschke and N. Chamel, in *The Physics and Astrophysics of Neutron Stars*, edited by L. Rezzolla, P. Pizzochero, D. Jones, N. Rea, and I. Vidaña, *Astrophysics and Space Science Library* Vol. 457 (Springer, Berlin, 2018), pp. 337–400.
- [13] A. K. Dutta, M. Onsi, and J. M. Pearson, *Phys. Rev. C* **69**, 052801(R) (2004).
- [14] M. Onsi, A. K. Dutta, H. Chatri, S. Goriely, N. Chamel, and J. M. Pearson, *Phys. Rev. C* **77**, 065805 (2008).
- [15] J. M. Pearson, N. Chamel, S. Goriely, and C. Ducoin, *Phys. Rev. C* **85**, 065803 (2012).
- [16] J. M. Pearson, N. Chamel, A. Pastore, and S. Goriely, *Phys. Rev. C* **91**, 018801 (2015).
- [17] A. Pastore, M. Shelley, and C. A. Diget, *PoS* **281**, 145 (2017).
- [18] A. K. Dutta, J.-P. Arcoragi, J. M. Pearson, R. Behrman, and F. Tondeur, *Nucl. Phys. A* **458**, 77 (1986).
- [19] K. Oyamatsu and M. Yamada, *Nucl. Phys. A* **578**, 181 (1994).
- [20] N. Chamel, S. Naimi, E. Khan, and J. Margueron, *Phys. Rev. C* **75**, 055806 (2007).
- [21] N. Chamel, *Phys. Rev. C* **85**, 035801 (2012).
- [22] C. J. Pethick and D. G. Ravenhall, *Annu. Rev. Nucl. Part. Sci.* **45**, 429 (1995).
- [23] D. G. Ravenhall, C. J. Pethick, and J. R. Wilson, *Phys. Rev. Lett.* **50**, 2066 (1983).

- [24] M. Hashimoto, H. Seki, and M. Yamada, *Prog. Theor. Phys.* **71**, 320 (1984).
- [25] R. D. Williams and S. E. Koonin, *Nucl. Phys. A* **435**, 844 (1985).
- [26] C. P. Lorenz, D. G. Ravenhall, and C. J. Pethick, *Phys. Rev. Lett.* **70**, 379 (1993).
- [27] C. J. Pethick and A. Y. Potekhin, *Phys. Lett. B* **427**, 7 (1998).
- [28] N. Martin and M. Urban, *Phys. Rev. C* **92**, 015803 (2015).
- [29] X. Viñas, C. Gonzalez-Boquera, B. K. Sharma, and M. Centelles, *Acta Phys. Pol. B* **10**, 259 (2017).
- [30] See Supplemental Material at <http://link.aps.org/supplemental/10.1103/PhysRevC.101.015802> for complete data files on which this paper is based.
- [31] M. Onsi, H. Przysieznik, and J. M. Pearson, *Phys. Rev. C* **55**, 3139 (1997).
- [32] N. Chamel and S. Goriely, *Phys. Rev. C* **82**, 045804 (2010).
- [33] S. Goriely and J. M. Pearson, *Phys. Rev. C* **77**, 031301(R) (2008).
- [34] M. Brack, C. Guet, and H.-B. Håkansson, *Phys. Rep.* **123**, 275 (1985).
- [35] J. Bartel, M. Brack, and M. Durand, *Nucl. Phys. A* **445**, 263 (1985).
- [36] Y. Kashiwaba and T. Nakatsukasa, *Phys. Rev. C* **100**, 035804 (2019).
- [37] P. Gögelein and H. Mütter, *Phys. Rev. C* **76**, 024312 (2007).
- [38] W. G. Newton and J. R. Stone, *Phys. Rev. C* **79**, 055801 (2009).
- [39] J. M. Pearson, Y. Aboussir, A. K. Dutta, R. C. Nayak, M. Farine, and F. Tondeur, *Nucl. Phys. A* **528**, 1 (1991).
- [40] C. Ducoin, Ph. Chomaz, and F. Gulminelli, *Nucl. Phys. A* **789**, 403 (2007).
- [41] N. Martin and M. Urban (private communication).
- [42] O. Y. Gnedin, D. G. Yakovlev, and A. Y. Potekhin, *Mon. Not. R. Astron. Soc.* **324**, 725 (2001).
- [43] G. Baym, H. A. Bethe, and C. J. Pethick, *Nucl. Phys. A* **175**, 225 (1971).
- [44] G. Watanabe, H. Sonoda, T. Maruyama, K. Sato, K. Yasuoka, and T. Ebisuzaki, *Phys. Rev. Lett.* **103**, 121101 (2009).
- [45] R. Ogasawara and K. Sato, *Prog. Theor. Phys.* **68**, 222 (1982).
- [46] B. Schuetrumpf, G. Martínez-Pinedo, M. Afibuzzaman, and H. M. Aktulga, *Phys. Rev. C* **100**, 045806 (2019).